Al 4 Ir: An Al–Ir Binary-Phase Superstructure of the Ni 2 Al 3 Type

Pascal Boulet, Marie-Cécile de Weerd, Emilie Gaudry, Saso Šturm, Julien Zollinger, Jean-Marie Dubois, Vincent Fournée, Julian Ledieu

Al4Ir: a new Al-Ir binary phase, superstructure of the Ni2Al3 type

Journal:	*Inorganic Chemistry*
Manuscript ID	ic-2022-00816t.R1
Manuscript Type:	Article
Date Submitted by the Author:	n/a
Complete List of Authors:	boulet, pascal; Institut Jean Lamour, UMR7198 CNRS-Université de Lorraine de Weerd, Marie-Cécile; Institut Jean Lamour, UMR7198 CNRS-Université de Lorraine Gaudry, Émilie; Institut Jean Lamour, UMR 7198 CNRS Université de Lorraine, Sturm, Saso; Institut Jozef Stefan, Department for nanostrucutred materials Dubois, Jean Marie; Institut Jean Lamour, UMR 7198 CNRS Université de Lorraine Zollinger, Julien ; Universite de Lorraine Fournée, Vincent; Institut Jean Lamour, UMR 7198 CNRS-Université de Lorraine Ledieu, Julian; Institut Jean Lamour, UMR7198 CNRS-Université de Lorraine

Al_4Ir: a new Al-Ir binary phase, superstructure of the Ni_2Al_3 type

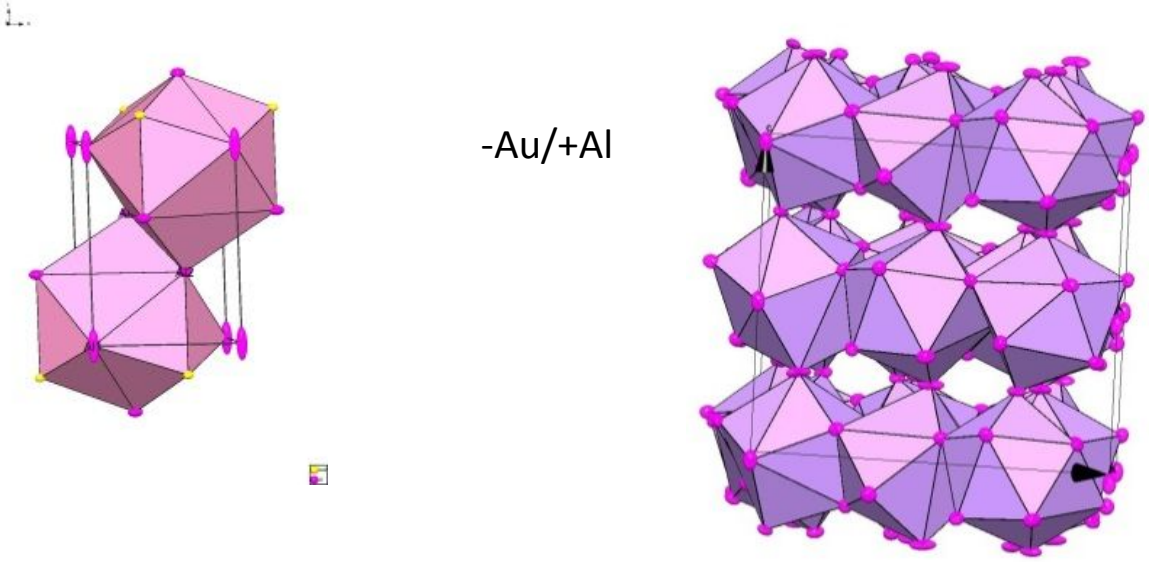

$AuIrAl_3$(Ni_2Al_3 type) Al_4Ir (Al_4Pd type)

Al_4Ir: a new Al-Ir binary phase, superstructure of the Ni_2Al_3 type

Pascal Boulet[1,3,], Marie-Cécile de Weerd[1,3], Emilie Gaudry[1,3], Saso Šturm[2,3], Julien Zollinger[1,3], Jean-Marie Dubois[1,2,3], Vincent Fournée,[1,3] Julian Ledieu[1,3]*

[1]Institut Jean Lamour, Université de Lorraine, CNRS, UMR 7198, 2 allée André Guinier, BP 50840, F-54000 Nancy, France

[2]Jozef Stefan Institute, Department for Nanostructured Materials, Jamova 39, SI-1000 Ljubljana, Slovenia

[3]International Associated Laboratory PACS2, Institut Jean Lamour, CNRS-Université de Lorraine, Nancy, FR -Institut Jožef Stefan, Ljubljana, SI.

Abstract

A new binary phase with composition Al_4Ir has been discovered in the Al-Ir binary system. Single crystal X-ray diffraction analysis reveals that it crystallizes in the trigonal space group *P3c1* with unit cell parameters: a = 12.8802(2) Å and c = 9.8130(2) Å. This structure is derived from the Ni_2Al_3 structure type. The supercell is due to the ordering of the aluminum atoms, which replace the nickel atoms in the prototype structure. The crystal structure was directly imaged by atomic-scale Scanning Transmission Electron Microscopy and the misalignment of the Al site responsible for the supercell has been clearly evidenced. Its metastable nature has been confirmed by Differential Thermal Analysis measurements. The atomic and electronic structures of Al_4Ir have also been investigated by Density Functional Theory. The structural optimization leads to lattice parameters and atomic positions in good agreement with the experimental ones. The compound is metallic, with a minimum in the density of states located more than 1 eV above the Fermi energy. This suggests a metastable system, in agreement with the electron count found much above 18 electrons per Ir atom, departing from the Hume-Rothery rule and with the presence of occupied antibonding states revealed by the Crystal Orbital Hamiltonian Population analysis. The relative stability of the compound is ensured by the hybridization between sp-Al and d-Ir states within Ir-centered clusters, while covalent-like interactions in between the clusters are indicated by the analysis of the Electron Localizability Function.

1. Introduction

Several binary phases were already reported in the Aluminum-Iridium system including the Al_9Ir_2, $Al_{45}Ir_{13}$, $Al_{13}Ir_4$, $Al_{28}Ir_9$, Al_3Ir, $Al_{2.7}Ir$ and AlIr compounds [1,2]. Several of these binary phases [3,4] exhibit complex structures from which interesting physical properties may emerge like the promising catalytic properties recently reported in $Al_{13}TM_4$ (M=Co, Fe, Ru) for example [5,6]. However, a more thorough investigation of the available literature reveals many uncertainties about the compound's exact composition as well as their real crystal structure. For example, Ode *et al.* [2] reported the existence of an unidentified phase in an as-cast Al-Ir sample with Ir concentration lower than 18.2 at%. This phase is also observed co-existing with Al in Al-Ir as-cast samples with compositions ranging from 2% to 10 at% Ir, and it disappears in favor of Al_9Ir_2 after annealing. Moreover, none of the diffraction peaks are indexed in the X-ray diffraction (XRD) pattern in the Al-18.2% Ir as-cast sample. For these reasons, we have reinvestigated the aluminum-rich part of the Al-Ir phase diagram. This paper will report on the precise description of a new Al-Ir binary phase, which we have characterized by Scanning Electronic Microscopy and Scanning Transmission Electronic Microscopy (SEM and STEM), X-ray diffraction (XRD on powder and single crystal), Differential Thermal Analysis (DTA) and Density Functional Theory calculations (DFT). The metastability of this new phase will be discussed based on these experimental measurements and theoretical calculations.

2. Experimental and Calculations details

Experimental details

The sample has been obtained by melting both elements in an arc-melting furnace under 0.6 bar of argon partial pressure. The starting materials were used in the form of ingots using Al shots (purity 99.9965% from Alfa Aesar and Iridium (purity 99.9% from Goodfellow) .The ingot obtained from the starting composition $Al_{98}Ir_2$ in atomic percent, was turned over and remelted four times to improve the sample homogeneity. The sample was studied by standard metallographic techniques, powder XRD using a Bruker D8 Advance diffractometer in Bragg-Brentano geometry with a monochromated $CuK\alpha_1$ wavelength, optical microscopy, SEM performed on a Quanta 650 FEG from FEI, combined with a Bruker Energy dispersive X-ray spectroscopy detector(EDS). Precipitates have been removed from the matrix by etching with diluted *aquaregia* (H_2O: 9; HNO_3: 1/3; HCl:2/3). The single crystalline precipitates analyses were performed on a Bruker Kappa Apex II diffractometer equipped with a mirror monochromator and a MoKα IμS microbeam (λ = 0.71073Å). The Apex 3-program package was used for the cell refinements and data reduction. The structure was solved using direct methods and refined with the SHELXL-2013 [7] and XSHELL [8] programs. Semi-empirical absorption correction (SADABS) was applied to the data. STEM investigations were carried out using a JEM - ARM 200F Cold FEG TEM/STEM operating at 200 kV and equipped with a spherical aberration (Cs) probe corrector, with a spatial resolution in STEM mode of 0.08nm.

Computational details

Electronic structure calculations were performed using the plane wave Vienna ab initio simulation package (VASP) [9-12]. We applied the projector-augmented wave (PAW) method [13-16], within the spin-polarized generalized gradient approximation (GGA-PBE). We considered atomic valences to be $3s^2\ 3p^1$ (Al) and $6s^1\ 5d^8$ (Ir). Total energies were minimized until the energy differences became less than 10^{-5} eV between two electronic cycles during the electronic structure calculations. Bulk calculations were performed using 550 eV cut-off energy (Ecut) and a Γ-centred 5×5×5 k-point grid. Electronic structure analysis was performed using Bader charges [17-19], density of states and

projected Crystal Orbital Hamilton Population (pCOHP) methods [20-23]. The charge spilling, i.e. electrons which cannot be projected onto the local basis, is found to be 2.3%. The structural parameters given by the XRD analysis, with all occupancies considered to be equal to 1, have been set as an initial guess for the structural optimization. Atomic structures were relaxed till the Hellmann-Feynman forces were as low as 0.01 eV/Å. They have been plotted using the VESTA software [24]

3. Results and discussions

3.1 Sample observation and new phase identification

SEM analysis performed on the as-cast sample, and powder XRD analysis (Figure 1) evidence the formation of a secondary phase embodied as needle precipitates in the Al matrix (Figure 2a). The EDS analysis revealed a composition of $Al_{80}Ir_{20}$ ±0.5at %, while the matrix corresponds to pure aluminium with additional submicrometre-sized Al-Ir precipitates (<1µm), not yet characterized. The X-ray powder pattern displayed in Figure 1, reveals the presence of the main phase indexed as aluminum face centred unit cell with a = 4.05 Å and other diffraction peaks that could not be indexed with any of the binary structures reported previously. Surprisingly, similar analysis performed using XRD and EDS by Hill *et al.* [25] on an arc-melted sample having the same starting composition point out a phase of different structure and composition.

@Figure 1 : X-ray powder pattern of the sample showing 2 phases: the aluminum (Fm-3m, with a = 4.05 Å) phase is identified by vertical blue lines while the vertical red lines indicate a possible indexation of the second phase as an hexagonal Ni_2Al_3 structure type with a = 4.29 Å and c = 4.89 Å.

@Figure 2: (a)On the left hand side, SEM-BSE pictures of the sample showing the formation of needle-like precipitate in the Al matrix. (b)The picture on the right hand side has been obtained after selective etching to remove the aluminium matrix.

3.2 Structural determination and characterization

A single crystal was obtained by crushing the as-cast sample obtained after etching as shown in Figure 2b. The crystal structure were solved from single crystal X-ray diffraction data to the trigonal *P3c1*(n°158) space group. The unit cell constants are a = 12.8802(2) Å and c = 9.8130(2) Å. The structure was solved by direct method (shelx-2013) and corresponds to 3 independent iridium atomic positions in 6d, 11 independent aluminium positions also in 6d, and 3 supplementary aluminium positions in 2c, 2b and 2a. Supplementary refinement cycles including the occupation factor of the atomic sites lead to a slightly deficient site for one aluminium position, giving a final composition of $Al_{3.99}Ir$ (Z=18), in agreement with the EDS measurement. The final anisotropic full matrix least square refinement on F^2 with 137 variables converged to R1 = 4.44%, Rw2 = 10.95% and a goodness of fit of 1.026. The complete crystallographic data are available in Table 1. The experimental atomic coordinates and isotropic displacement parameters are shown in Table 2, and the Table 3 displays the anisotropic displacements for each crystallographic sites. The complete crystallographic data are available at the Cambridge Crystallographic data centre under the number CCDC 2157020. Figure 3 displays the crystal structure obtained, showing the Ir coordination polyhedron with the Al thermal ellipsoids.

@ Table 1: Crystallographic data for Al_4Ir

@Table 2: Experimental atomic coordinates and isotropic displacement parameters. The numbers in italics correspond to the atomic coordinates after relaxation.

@table 3 **:** Anisotropic atomic displacement parameters ($Å^2$) for Al_4Ir

@ Figure 3: Crystal structure of Al_4Ir showing the Ir polyhedron in the (ab) plane (hight) and in the (ac) plane (down).

The crystal structure consists of layers of edge and face sharing Al10-polyhedra, centred by Ir atoms. For the three Ir sites, polyhedra correspond to a distorted square based pyramid with 10 different Al-Ir distances ranging from 2.5 Å to 2.7 Å. The layers of polyhedra are thus stacked along the crystallographic c-axis and connected by common corners. A search for parent compounds from a data-base of inorganic compounds revealed that Al_4Ir crystallizes with a structure similar to that of Al_4Pd [26] and Al_4Pt [27]. However, in the case of the Pt containing compound, supplementary deficient sites were observed for aluminium atoms. Subsequent refinements were performed adding these 4 atomic positions, but this did not improve our model. As mentioned in the case of Al_4Pt, the unit cell adopted by these systems correspond to a superstructure with a_{Al4X} = 3a of the subcell type and c_{Al4X} = 2c of the subcell type, the subcell type being that of Ni_2Al_3. Note that we have recently reported the existence of a new ternary phase $AuIrAl_3$ also with the Ni_2Al_3 structure-type [28]. Figure 4 displays the precession images obtained for both $AuIrAl_3$ and Al_4Ir structures. At the upper level, the precession along c* for the two structures is displayed. In both cases, similar strong reflections are observed whereas in the case of the binary Al_4Ir structure, weak superstructure reflections are observed at respectively 1/3 and 2/3. At the lower level of the picture, precession images along b*, confirm the behaviour along the a* axis (and b*) whereas no other supplementary reflections are observed along the c* axis on the zero layer (not shown here). Conversely, on the first layer, additional spots are observed at ½ positions, indicating a doubling of the unit cell along the c direction. This behaviour is explained by the c glide plane (l = 2n, for (00l) and (h-hl)) observed in the case of *P3c1* adopted for the binary structure and not in *P-3m1* adopted for the ternary $AuIrAl_3$ [28].

@ Figure 4: comparisons of precession images obtained for $AuIrAl_3$ (Ni_2Al_3 type) and the Al_4Ir superstructure.

The existence of the superstructure lies in the deviation of the Ir atomic positions from the ideal hexagonal primitive stacking observed for the ternary structure. The above described superstructure was additionally studied by the atomic-scale STEM imaging technique combined with a high-angle annular dark-field (HAADF) detector (Figure 5). In this imaging mode the contrast variation in the atomic-resolution, the so-called Z-contrast images, is roughly following a Z^2 dependence on the average atomic number of the probed atom column. Consequently, the intensity of HAADF-STEM images reflects compositional variations at the atomic scale. Only Ir atomic columns are clearly visible in the experimental HAADF-STEM image. The Al columns cannot be resolved, which is due to the lower atomic number of Al (13) when compared to Ir (77) and the small projected distance between neighbouring Al columns, beyond the given spatial resolution of the electron probe.

@Figure 5: (a) Experimental atomic-scale HAADF-STEM image. (b) Low frequency filtered image with Ir atomic planes highlighted with higher intensity (marked by an arrow).

The weak, slowly varying contrast that extends over large areas in the image is an artefact originating from the partly amorphized specimen surface induced during TEM specimen preparation. An important feature that can be observed in the experimental HAADF-STEM image is characterized by a periodic variation of contrast between sets of (010) lattice planes, so that every third (010) lattice plane

appears brighter when compared with the two sandwiched lattice planes. To quantitatively determine the variation of the described contrast, first the experimental HAADF-STEM image was filtered by removing the low frequency noise (Figure 5b), followed by a 3.6 nm long line profile, which is averaged over the width of 3.6 nm perpendicular to the (010) lattice planes (Figure 6). The periodic contrast variations between neighbouring planes are clearly visible. This phenomenon can be directly related to the underlying crystal structure. Namely, Ir atoms in atomic columns are well aligned only in every third (010) lattice plane, while in the remaining two neighbouring lattice planes Ir atoms undulate around the central position of the corresponding atomic columns, resulting in a relatively lower overall intensity.

@Figure 6: Intensity profile perpendicular to (010) Al_4Ir lattice planes

To shed more light on this new phase, DTA was carried out on the as cast sample from 100°C to 1200°C with heating and cooling rates of 20 K.min-1, and repeating the cycle one time, (Figure 7), confirm the metastability of this new binary phase. The two curves obtained present an endothermic peak at about 660°C but are not similar. The first one presents a double peak with onset at 660°C and 675°C, and a heat of 24µV.s/mg. The second curve presents a single peak with a heat of 33 µV.s/mg. On cooling (not shown in the figure), only one peak is observed in both measurements which confirms the disappearance of the binary phase during the second heating. This is further confirmed after the DTA measurement, where the sample was slowly cooled to room temperature since, all diffraction peaks from this new Al_4Ir phase were absent in favour of the appearance of diffraction peaks of the Al_9Ir_2($P2_1/c$)[29], $Al_{45}Ir_{13}$ (Pnma)[4] and $Al_{28}Ir_9$(P31c)[3]. The figure 8 displays the XRD diagram with the position of all diffraction peaks obtained from the ICDD 2022 database [30] with the published data of Al_9Ir_2-PDF 04-011-7686, $Al_{45}Ir_{13}$-PDF 04-011-8151 and $Al_{28}Ir_9$-PDF 04-013-5108 and Al – PDF 04-012-7848 in ref. 31.

@Figure 7: Differential thermal analyses (a) first heating , (b) second heating

@Figure 8 : X-ray powder pattern of the sample after the DTA measurements showing 4 phases: the aluminum (Fm-3m, with a = 4.04 Å) phase is identified by vertical blue lines while the vertical red lines indicate Al_9Ir_2 ($P2_1/c$), the black ones $Al_{45}Ir_{13}$ (Pnma) and the light blue ones to $Al_{28}Ir_9$(P31c).

4. DFT calculations

The optimization of the XRD structure leads to cell parameters in good agreement with the experimental data, while slightly larger by approx. 0.5% (see Table 1). A good agreement is also found for the atomic positions (Table 2). It is worth mentioning that the difference between the calculated and the experimental xyz values are larger for atoms showing a larger thermal isotropic factor, namely Al(5) and Al(6). The value obtained for Al(5) is probably related to its partial occupancy. But such an argument is not valid for Al(6), since a full occupancy has been experimentally found.

The electronic density of states of Al_4Ir is plotted in Figure 9. The Al-s states show a non-negligible contribution below -4 eV, while Al-p states and Ir-d states are mostly found above -6 eV. The compound is metallic. The presence of Ir-d and Al-sp states located at similar energies suggest orbital hybridization. This is further confirmed by the COHP analysis, which highlights Al-Ir bonding states within [-11; -2] eV. The cohesion of the Al_4Ir phase is also ensured by interactions in between the Ir-centered clusters, as shown by the presence of Electron Localization Factor isosurfaces with an isodensity larger than 0.7, in the planes z=0.25 and z=0.75, pointing along the shortest Al-Al pairs

(d=2.82 Å), thus suggesting the shortest Al-Al bonding with a covalent-like character (Fig 10). The Bader charge analysis reveals that the average charge carried by Al atoms is +1.2e, while Ir atoms are negatively charged (-4.8e). All together, these results show that the bonding network of the Al_4Ir compound is a combination of iono-covalent and metallic interactions.

@Figure 9: Density of states of bulk Al_4Ir. Black = Total DOS, green/blue = Al s/p contribution, red = Ir contribution.

@ Figure 10: Electron Localization function, showing the isodensity larger than 0.7 (in red) between two aluminum atoms

Several features in the electronic structure suggest that Al_4Ir is metastable. First, the electron count does not match with the 18-n counting rule, where *n* is the number of electron pairs shared among transition metals within multicenter interactions. Considering that Iridium atoms are isolated from each others in Al_4Ir (n=0), since the distance between neighboring Ir atoms is quite large (4.37 Å), and according to the electronic configurations of Ir and Al, the average number of electron per Ir atoms is found to be 21, i.e. well above the optimized electron count (18). Second, the Hume-Rothery matching rule $2k_F = G$, where k_F is the Fermi wave vector calculated within the nearly free electron model (NFE), and G is a reciprocal vector, can hardly apply here. We found $2\ k_F = 3.45\ A^{-1}$, which does not coincide with intense Bragg peak positions in the X-ray diagram. It is worth noticing that the value found for k_F within the NFE model is much lower than the one given by DFT ($k_F^{DFT}=1.98\ A^{-1}$), in agreement with the polar character of the Al_4Ir intermetallic compound. At least, the COHP analysis also suggests a possible metastable character for Al_4Ir. Indeed, the Al-Ir averaged COHP shows a non-negligible contribution of occupied antibonding states, within the energy range [-2, 0] eV. Similarly, the Al-Al averaged contributions in the range [0, 1] eV present a small bonding character (Fig 11).

@Fig. 11 : (a) COHPs for Al-Al and Al-Ir bonds averaged over all Al-Al and Al-Ir bonds shorter than 3A ; (b) COHPs for the shortest Al-Al bonds (2.640 Å)

5. Discussion

As mentioned in the structure description, this large hexagonal structure corresponds to a superstructure of the well-known Ni_2Al_3 structure type, which we have reported for the ternary phase $AuIrAl_3$ [28]. Figure 1 shows that the main diffraction peaks of this phase correspond to the Ni_2Al_3 type of unit cell with a = 4.29 Å, c = 4.89 Å and V = 78.3 $Å^3$. For comparison, the unit cell dimensions of the ternary $AuIrAl_3$ are a = 4.2584(5) Å, c = 5.1991(7) Å and V = 81.65 $Å^3$. With Au and Ir atoms sharing similarities (atomic radius, crystal structure…), with only 2 electrons difference, they both randomly occupy the Ni sites. Thus, replacing Au atoms by Al atoms in the ternary phase, leads to a clear evidence of superstructure for the binary Al_4Ir phase corresponding to $a_{Al4Ir} = 3a_{Al3AuIr}$ and $c_{Al4Ir} = 2c_{Al3AuIr}$. Ab initio calculation points toward an $AuIrAl_3$ phase stabilized by a Hume-Rothery mechanism. The stability of this structure was recently established by the 18-n rule [32], indicating that the isolobal Au(Ir)-Au(Ir) bond concept can also be used to interpret electron localization along the Al-bridged Ir-Au contact in the Al_3AuIr compound. In the case of the binary Al_4Ir, replacing one Au atom by one Al atom results in a considerable change. The Fermi wave vector is approximated, using a free electron model to $2k_F = 3.45\ Å^{-1}$, which contrarily to the $AuIrAl_3$ system does not coincide with intense Bragg peak positions in the X-ray diagram. The electron count is obviously reduced by the Au substitution by Al, which destabilizes the Ni_2Al_3 structure type, by tilting the icosahedra towards each other as shown in Figure 4. So the 18 electrons rule is not followed in the case of Al_4Ir. For such reasons, the Al_4Ir is observed only in the XRD as-cast sample and disappears after the second heating of the DTA measurements

The relative stability of the compound is ensured by the hybridization between sp-Al and d-Ir states within Ir-centered clusters, while covalent-like interactions in between the clusters are suggested by the analysis of the Electron Localizability Function. For these reasons the Al_4Ir phase exhibits a small thermal homogeneity range which should occur at very high temperature below the liquidus curve.

The binary system Al-Ir is definitely an interesting system showing the existence of a variety of phases with different crystalline structures. Al_4Ir(P3c1) is a Ni_2Al_3 type (P-3m1) derivative because P3c1(158) space group can be considered by two transformations as one of the subgroup of the P-3m1, based on Bärnighausen tree formalism[33], and as shown the table 4. In the $AuIrAl_3$ structure, Al occupy the special Wyckoff site 1a(0,0,0) and 2d(1/3,2/3, z)and the (Au, Ir) atoms occupy another 2d site . By multiplying the c axis of $AuIrAl_3$ by 2, the Wyckoff positions split in the Wyckoff positions of the subgroup P-3c1(165), with 1a splitting in 2b, and the two 2d positions in two 4d. By applying a second transformation and multiplying by 3 the parameters of the hexagonal basal plane, a' = 3a and b'= 3b, each position are split in Wyckoff position from the subgroup P3c1(158) with the splitting display in table 4. The 2a is split in three 6d position and each 4d positions lead to 4 x 6d positions and 2a 2b and 2c. The result lead the same number of 90 atoms in the unit cell, with 13 6d positions, instead of 14 in our model and 2 times the sequence (2a, 2b and 2c) Wyckoff positions instead of one found experimentally.

@table 4 : Barnighausen tree showing the relationship between P-3m1 adopted for $AuIrAl_3$, P-3c1, P3c1 adopted for Al_4Ir.

Furthermore, comparing the Al_4Ir crystal unit cell with those reported for $Al_{28}Ir_9$ (P31c)[3] where a = 12.2864(4) Å and c = 27.341(1) Å, show close resemblance with both structures with similar a lattice and $cAl_4Ir \approx 1/3\ cAl_{28}Ir_9$. However contrary to AuIrAl3, this evidence with $Al_{28}Ir_9$ could not be explain yet using Bärnighausen formalism.

In all the Al-Ir binary phases reported yet with Al4Ir, Ir-centered clusters with aluminium surrounding indicated interatomic distances around 2.5, which corresponds to short distance smaller than the addition of both atomic radius, and shorter than Ir-Ir or Al-Al usual interatomic distances. This observation with the covalent interaction suggested by the Electron Localization Function of Al4Ir but with also the polar character deduced from the Bader charge analyses indicate that Al_4Ir and probably other Al-Ir binary and ternary phase should belong to the polar intermetallic phases as presented by Corbett J.D [34]. This behavior should be discuss in a more general paper concerning the reinvestigation Al-Ir binary phases diagram perform by people from our network soon.

The stability of these phases seems also to be an interesting subject to look at. In the Al-Au-Ir ternary system for instance, 2.5 at.% of gold is sufficient to form a phase with a new crystalline structure [35], not observed in the Al-Ir binary system. A comparable situation was also found in the Al-Ir-Si system [36]. Finally anomalous effect of Cu-doping on structural and thermoelectric properties of Al-Ir cubic quasicrystalline approximant has also been reported recently [37]. These results should motivate further experimental and numerical studies in the Al-Ir-X systems aiming to find new compounds exhibiting unique physical and chemical properties and to improve the understanding of the stabilization mechanisms in these materials.

6. Conclusions

In agreement with the latest Al-Ir binary system investigations [2,3,4], we have solved the crystal structure of a new metastable Al-Ir phase. This phase corresponds to Al_4Ir crystallizing into a large hexagonal unit cell corresponding to a volume of 18 times that of the pseudo Ni_2Al_3 structure type. However this phase is only observed in the as cast sample and disappears after very short time annealing. All experimental technique used such as XRD and DTA confirmed the metastable behavior of this phase. Comparing the crystal structure with that of a very similar ternary $AuIrAl_3$ phase, obtained by an exchange of a gold atom by aluminum illustrates the huge effect of this chemical substitution on the electronic structure and phase stability of the compounds. Contrary to the ternary phase, the stabilization mechanism of the binary Al_4Ir phases cannot be explained by the usual Hume-Rothery or 18 electrons rules. Indeed, Crystal Orbital Hamilton Population calculation indicates a non-negligible contribution of occupied antibonding states, which explain the metastable nature of the new binary phase.

Acknowledgment

This work was performed in the frame of the International Research Project (IRP) $PACS_2$. The research was financially supported by Slovenian Research Agency (P2-0084), CNRS and Université de Lorraine, France, and the European Union Horizon 2020 research and innovation program under grant agreement No. 823717 – ESTEEM3.

We acknowledge financial support through the COMETE project (COnception in silico de Matériaux pour l'EnvironnemenT et l'Energie) co-funded by the European Union under the program FEDER-FSE Lorraine et Massif des Vosges 2014-2020. This work was granted access to the HPC resources of TGCC, CINES and IDRIS under the allocation 99642 attributed by GENCI (Grand Equipement National de Calcul Intensif). High Performance Computing resources were also partially provided by the EXPLOR centre hosted by the University de Lorraine (project 2017M4XXX0108).

References

[1**]** Okamoto, H. Al-Ir (Aluminium-Iridium). J Phase Equili. Diffus. 30 (2009) 206-207.

[2] Ode M., Abe T., Murakami H., Yamabe-Mitarai Y., Hara T., Nagashio K., Kocer C. and Onodera H. An Investigation of the phase diagram of the Al-Ir binary system. Intermetallics 16 (2008) 1171.

[3] Katrych S., Gramlich V. and Steurer W, Trigonal Ir9Al28, a new structure type and approximant to decagonal quasicrystals. J. Alloys Compd. 407 (2006) 132.

[4] Boström M., Niewa R., Prots Y.M., Grin Y., Synthesis, phase relationship and crystal structure of the new binary compound Ir13Al45. J. Solid State Chem. 178 (2005) 339.

[5] Piccolo L., Chatelier C., De Weerd M.C., Morfin F., Ledieu J., Fournée V., Gille P., Gaudry E., Catalytic properties of Al13TM4 complex intermetallics: influence of the transition metal and the surface orientation on butadiene hydrogenation. Science and Technology of Advanced Materials, 20 :1 (2019) 557

[6] Armbrüster M., Kovnir K., Friedrich M., Teschner D., Wowsnick G., Hahne M., Gille P., Szentmiklosi L., Feuerbacher M., Heggen M., Girgsdies F., Rosenthat D., Schlögl R., Grin Y.,

Al13Fe4 as a low-cost alternative for palladium in heterogeneous hydrogenation. Nature Materials 11 (2012) 690.

[7] Sheldrick, G.M. A short history of SHELX. Acta Crystallograph., Sect. A, : Found Crystallogr, 64 (2008) 112-122.

[8] XSHELL © 2004 Bruker AXS version 6.3.1.

[9] Kresse, G., Hafner, J.,Ab initio molecular dynamics for liquid metals, Phys. Rev. B, 47 (1993) 558–561.

[10] Kresse, G., Hafner, J.,Ab initio molecular-dynamics simulation of the liquid-metal-amorphous-semiconductore transition in germanium, Phys. Rev. B, 49 (1994) 14251–14269.

[11] Kresse, G.; Furthmüller, J, Efficiency of ab-initio total energy calculations for metals and semiconductors using a plane-wave basis set, Comput. Mater. Sci., 6 (1996) 15–50.

[12] Kresse, G.; Furthmüller, J, Efficient iterative schemes for ab initio total-energy calculations using a plane-wave basis set, Phys. Rev. B, 54 (1996) 11169 – 11186.

[13] Blöchl, P. E., Projector augmented-wave method, Phys. Rev. B, 50 (1994) 17953.

[14] Kresse, G.; Joubert, D. , From ultrasoft pseudopotentials to the projector augmented-wave method, Phys. Rev. B, 59 (1999) 1758.

[15] Perdew, J. P.; Burke, K.; Ernzerhof, M., Generalzed Gradient Approximation Made Simple, Phys. Rev. Lett., 77 (1996) 3865.

[16] Perdew, J. P.; Burke, K.; Ernzerhof, M. , Generalized Gradient Approximation Made Simple, Phys. Rev. Lett. 78 (1997) 1396.

[17] Henkelman G., Arnaldsson A., and Jónsson H. A fast and robust algorithm for bader decomposition of charge density. Comput. Mater. Sci., 36:254–360, 2006.

[18] Tang W., Sanville E., and Henkelman G. A grid-based Bader analysis algorithm without lattice bias. J. Phys. Condens. Matter, 21:084204, 2009

[19] Yu M. and Trinkle D. R. Accurate and efficient algorithm for Bader charge integration. J. Chem. Phys., 134:064111, 2011.15, 16]

[20] Maintz S., Deringer V. L., Tchougréeff A. L., and Dronskowski R. Analytical projection from plane-wave and PAW wavefunctions and application to chemical-bonding analysis in solid. J. Comput. Chem., 34:2557–2567, 2013

[21] Maintz S., Deringer V.L., Tchougreeff A.L., and Dronskowski R. LOBSTER: A Tool to Extract Chemical Bonding from Plane-Wave Based DFT. J. Comput. Chem., 37:1030–1035, 2016

[22] Deringer V.L., Tchougreff A.L., and Dronskowski R. Crystal orbital hamilton population (COHP) analysis as projected from plane-wave basis sets. J. Phys. Chem. A, 115:5461–5466, 2011

[23] Dronskowski R. and Blöchl P.E. Crystal orbital Hamilton population (COHP): energy-resolved visualization of chemical bonding in solids based on density-functional calculations. J. Phys. Chem., 97, 33, 8617–8624, 1993.

[24] Momma K. and Izumi F. VESTA 3 for Three-Dimensional Visualization of Crystal, Volumetric and Morphology Data. J. Appl. Crystallogr., 44:1272–1276, 2011

[25] Hill P.J., Cornish L.A. and Witcomb M.J., Constitution and hardnesses of the Al-Ir system, Journal of Alloys and Compds, 280 (1998) 240-250.

[26] Yurechko M., Fattah A., Velikanova T. and Grushko B.,A contribution to the Al-Pd phase diagram, Journal of alloys and Compds, 329 (2001) 173.

[27] Wörle M., Krumeich F., Chatterji T, Kek S., and Nesper R.,On the structure and twinning of PtAl4, Journal of alloys and Compds 455 (2008) 130.

[28] Kadok J., de Weerd MC., Boulet P., Gaudry E., Grin Y., Fournée V. and Ledieu J., Al3AuIr : A new Compound in the Al-Au-Ir system, Inorg. Chem, 54 (2015) 16, 7898.

[29] Bostrom M, Rosner H., Prots Y.M., Burkhardt U. Grin Y., The Co2Al9 structure type revisited" Z. Anorg. Allg. Chem. 2005, 631, 534.

[30] ICDD, International Centre for Diffraction Data, PDF4+ 2021

[31] Muts N., Gladyshevskii R.E., Gladyshevkii E.I., Crystal structure of the compounds PrAl2Si2, Pr3Al4Si6 and PrAlSi2, J. Alloys Compds 2005, 402, 66

[32] Yannelo V.J.and Frederickson D.C., Generality of the 18-n Rule: Intermetallic Structural Chemistry Explained through Isolobal Analogies to Transition Metal Complexes, Inorg. Chem, 54 (2015) 11385-11398.

[33] Bärnighausen H. Group-subgroup relations between space groups: a useful tool in crystal chemistry. Commun Math Comput Chem 1980;9:139–75.

[34] Corbett J.D. Exploratory Synthesis: The fascinating and diverse Chemistry of polar intermetallic phases, Inorg. Chem 2010, 49, 13-28

[35] Kadok J., de Weerd M.C., Boulet P., Fournée V., Ledieu J., A new ternary compound with the BGa8Ir4 structure type in the Al-Au-Ir system. Acta Cryst B75 (2019) 49.

[36] Kadok J. et al, private communication 2021.

[37] Iwasaki Y., Kitahara K., Kimura K., Anomalous effect of the Cu-doping on structural and thermoelectric properties of the Al-Ir cubic quasicrystalline approximant. J. Alloys Compd 763 (2018) 78.

Table captions

Table 1: Crystallographic data for Al_4Ir

Table 2: Experimental Atomic coordinates and isotropic displacement parameters, the number in italics correspond to the atomic coordinates after relaxation**.**

Table 3 : Anisotropic atomic displacement parameters ($Å^2$) for Al_4Ir

Figure Caption

Figure 1 : X-ray powder pattern of the sample showing 2 phases: the aluminium (Fm-3m, with a = 4.05 Å) phase is identified by vertical blue lines while the vertical red lines indicate a possible indexation of the second phase as an hexagonal Ni_2Al_3 structure type with a = 4.29 Å and c = 4.89 Å.

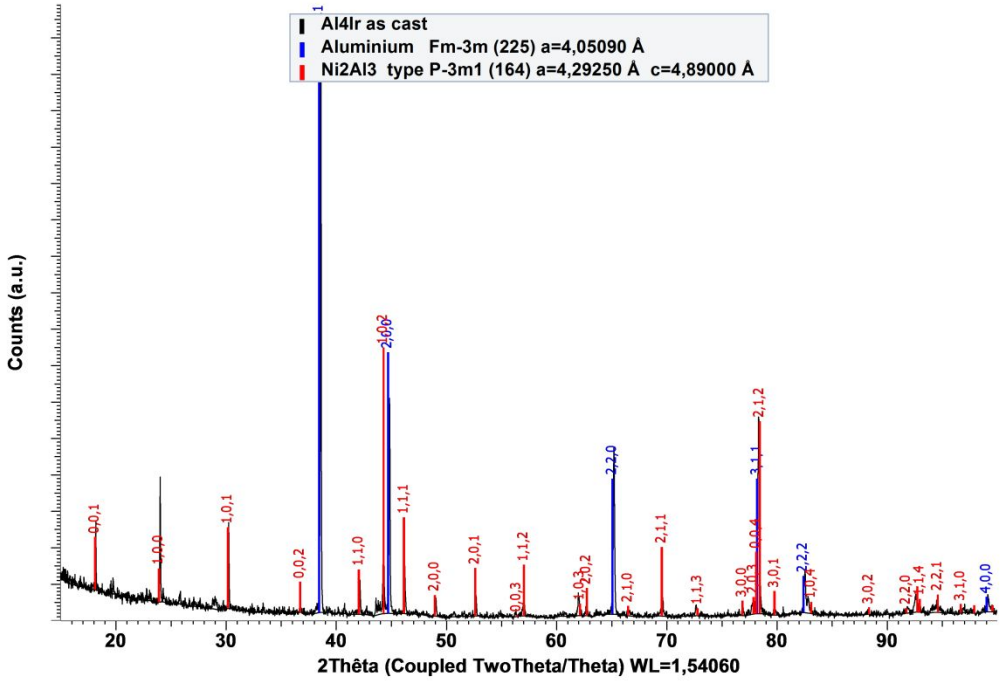

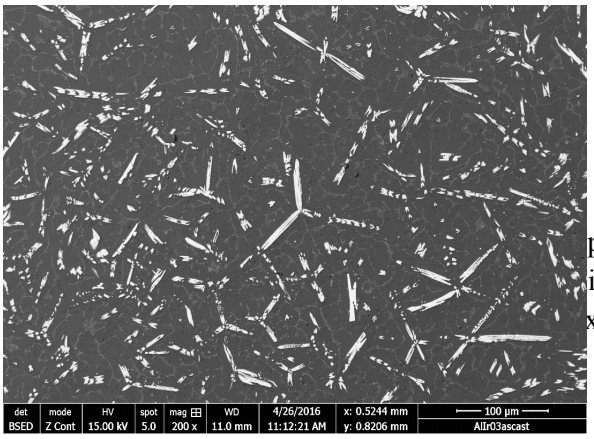

pictu

ictur

x.

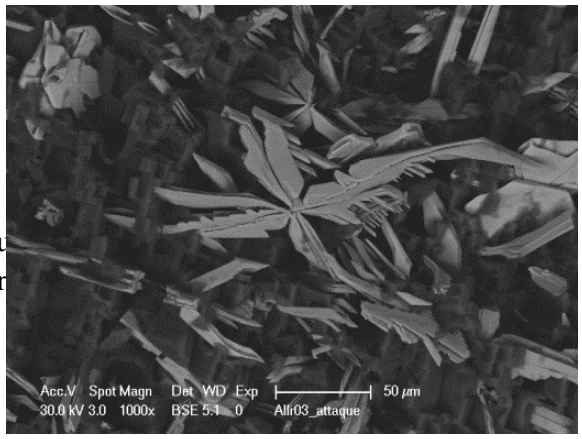

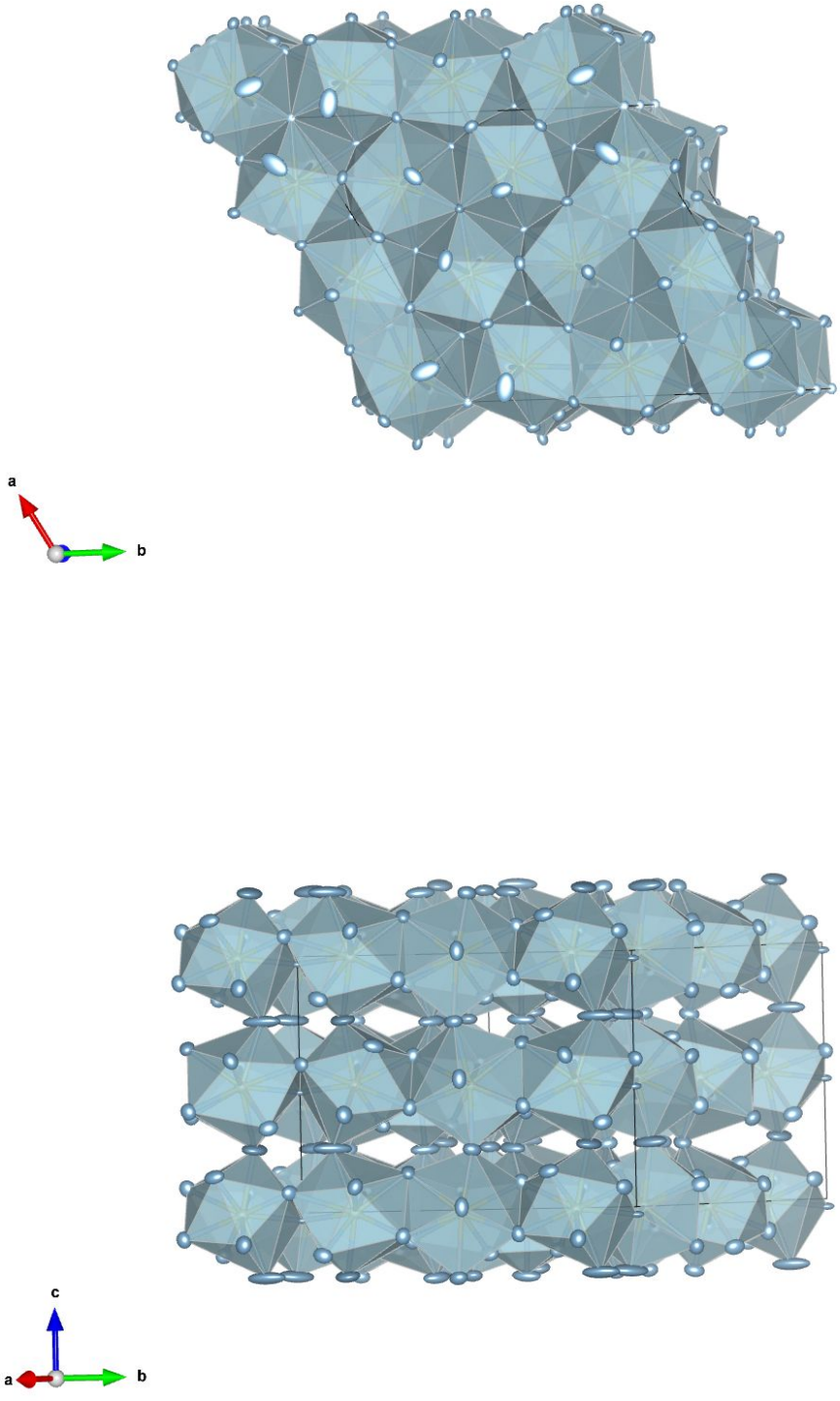

@Figure 3: Crystal structure of Al_4Ir showing the Ir polyhedron in the (ab) plane (high) and in the (ac) plane (down). Only Aluminium ellipsoid atoms are visible

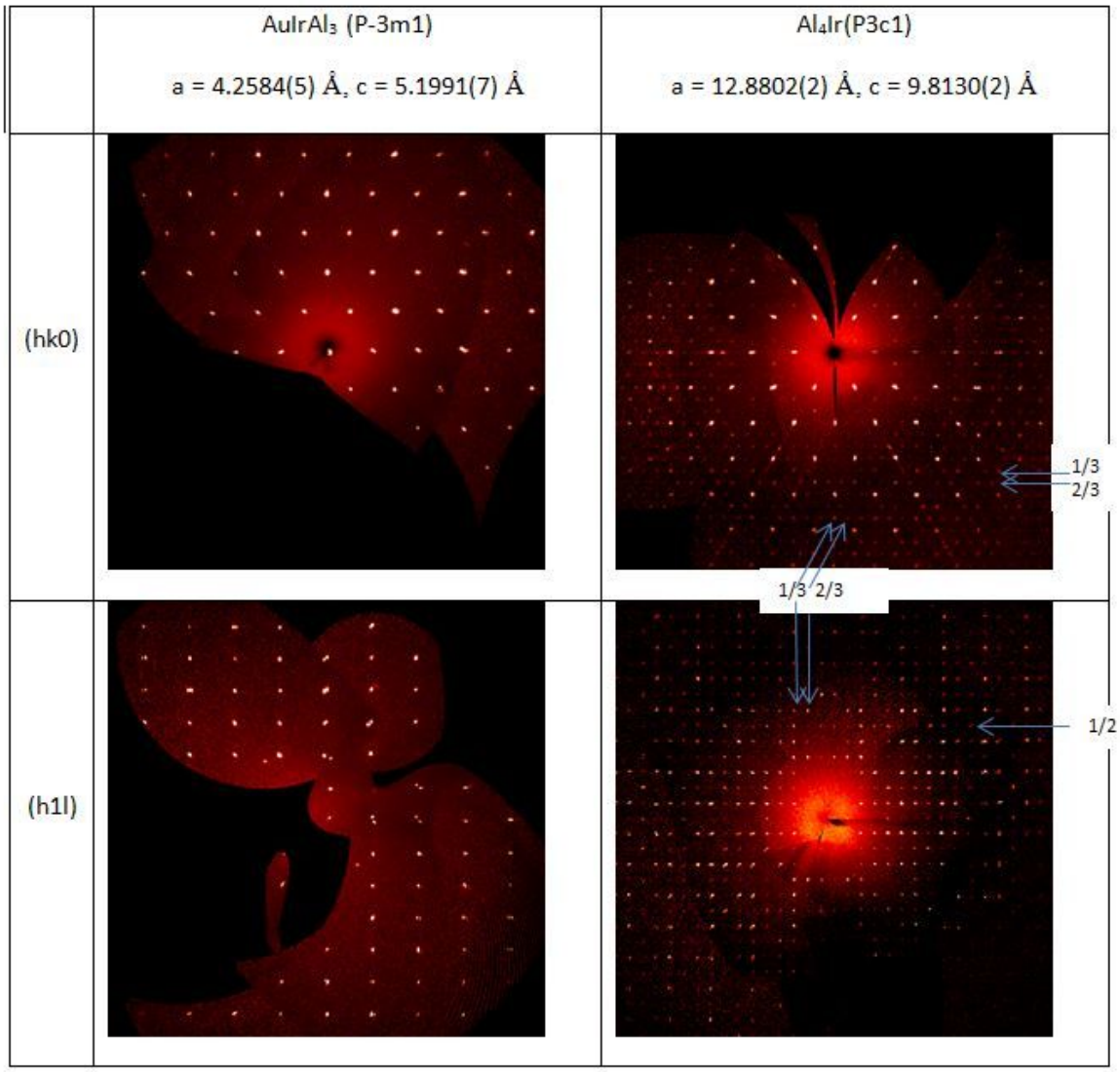

@Figure 4: Comparison of precession images obtained for Al_4Ir as a superstructure of the $AuIrAl_3$ phase (Ni_2Al_3 type).

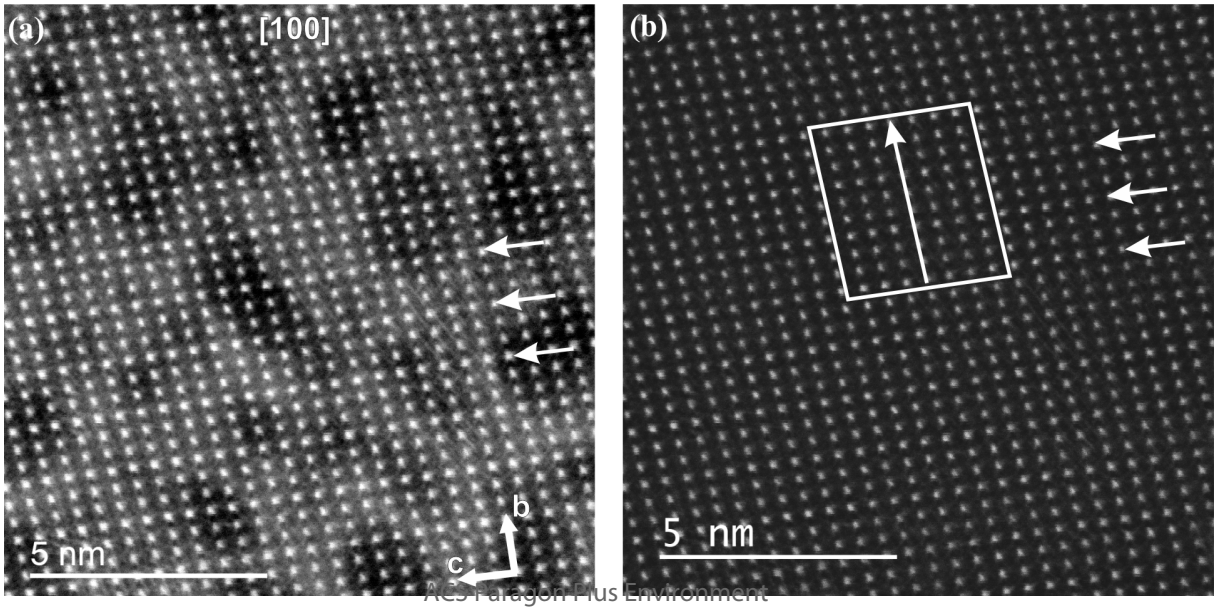

@Figure 5: (a) Experimental atomic-scale HAADF-STEM image. (b) Low-frequency filtered image with indicated atomic planes with higher intensity (marked by arrows).

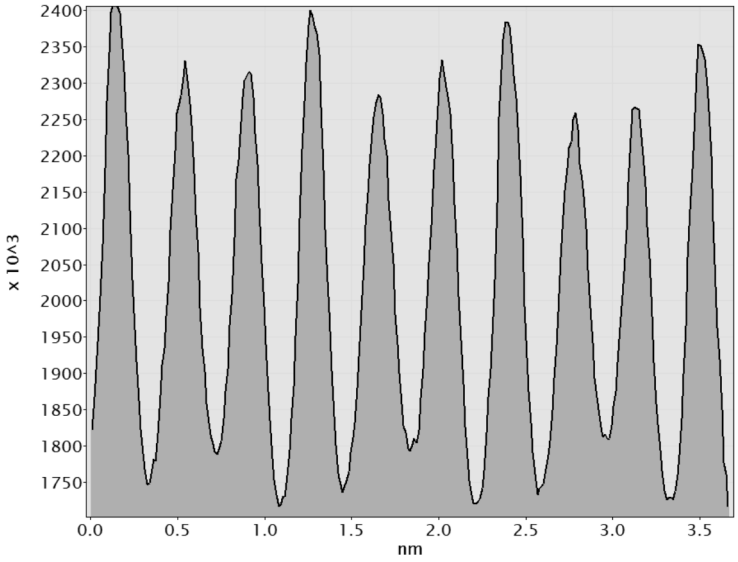

@Figure 6: Intensity profile perpendicular to (010) Al_4Ir lattice planes.

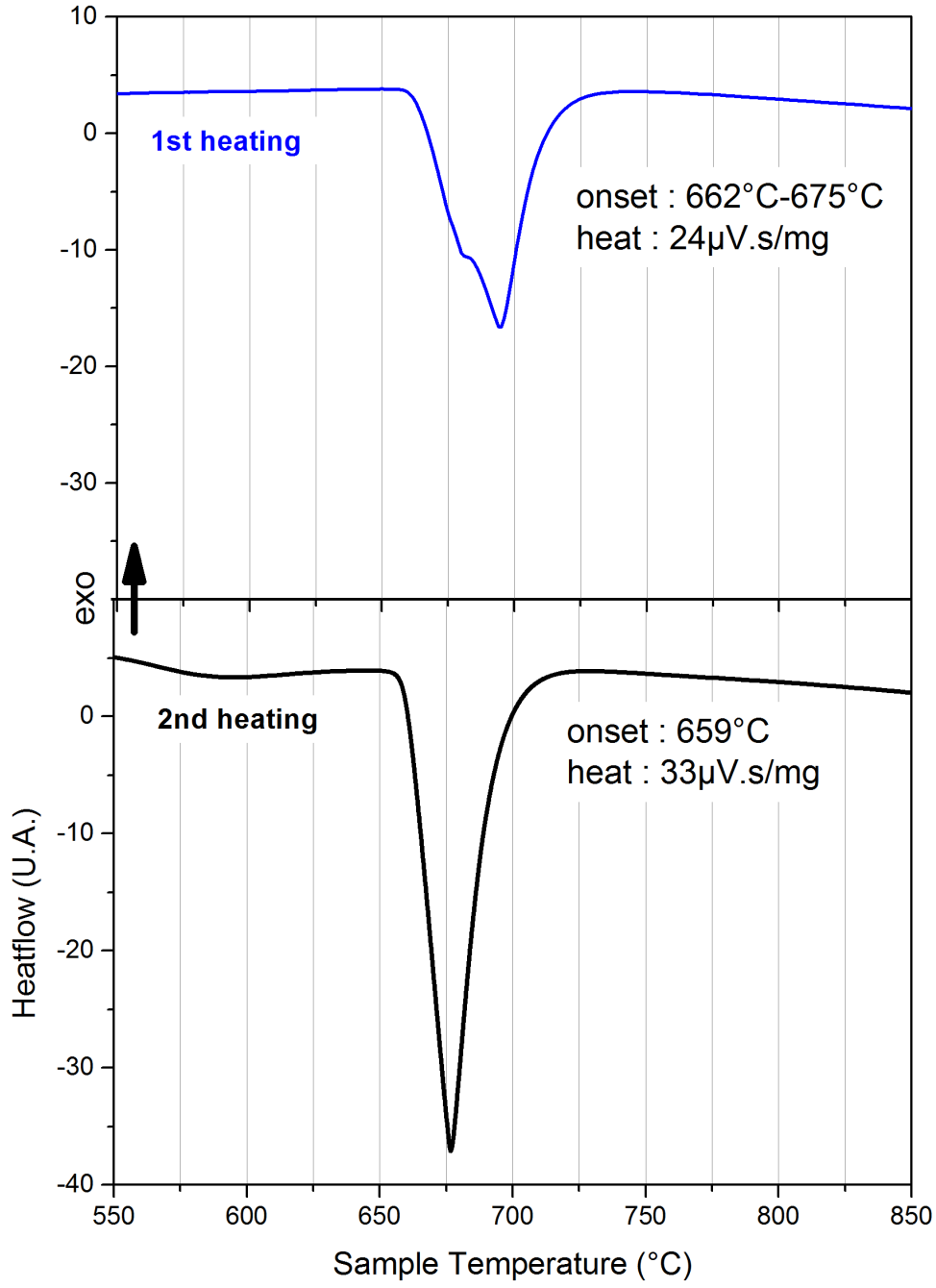

@Figure 7: Differential thermal analyses (a) first heating , (b) second heating

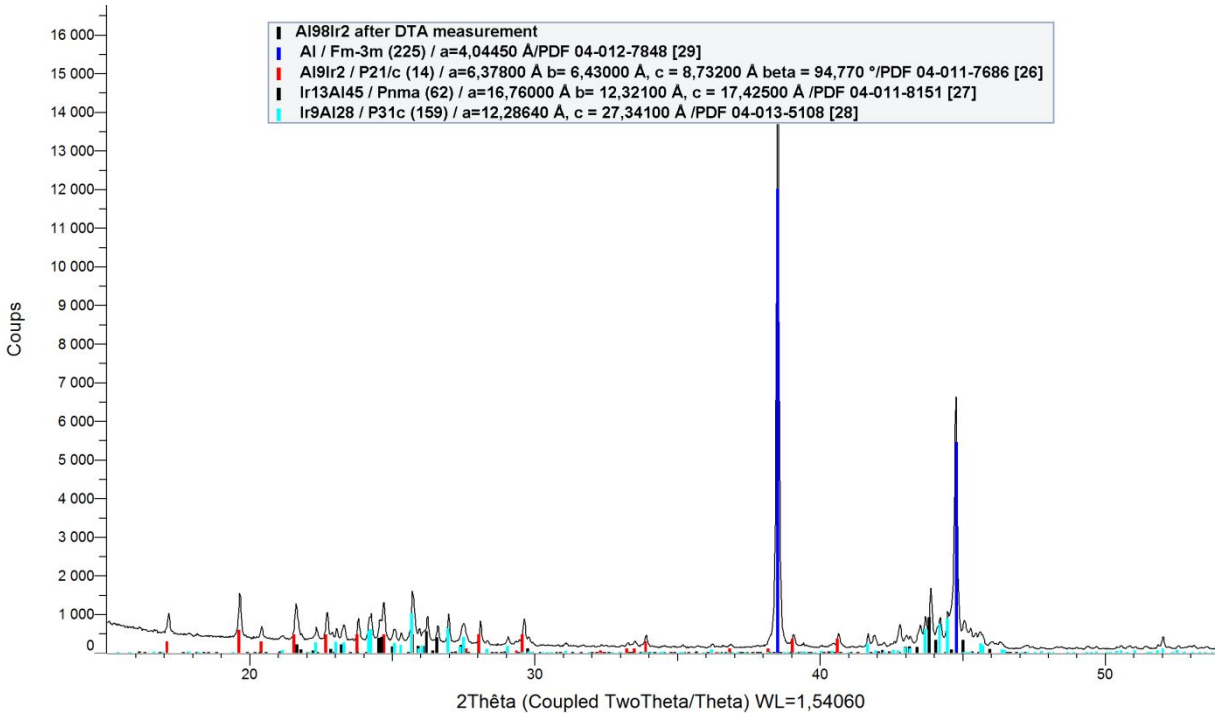

@Figure 8 : X-ray powder pattern of the sample after the DTA measurements showing 4 phases: the aluminum (Fm-3m, with a = 4.04 Å) phase is identified by vertical blue lines while the vertical red lines indicate Al_9Ir_2 ($P2_1/c$), the black ones $Al_{45}Ir_{13}$ (Pnma) and the light blue ones to $Al_{28}Ir_9$(P31c).

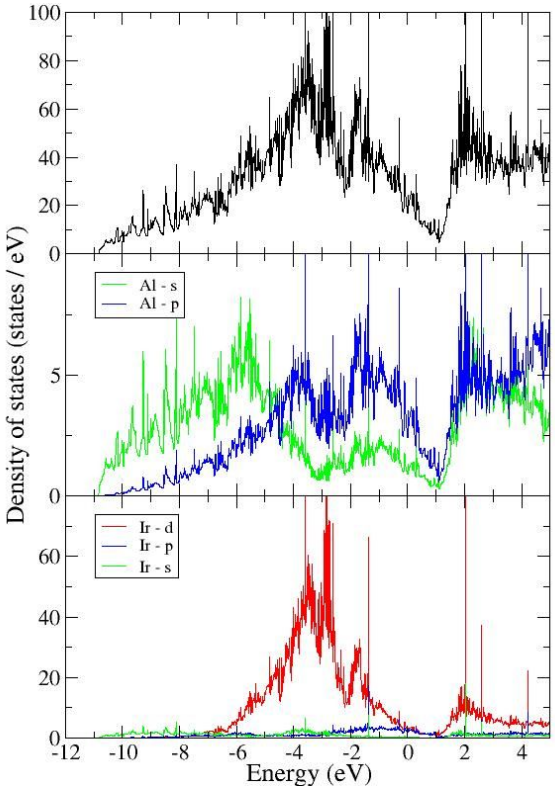

@Figure 9: Density of states of bulk Al_4Ir. Black = Total DOS, green/blue = Al s/p contribution, red = Ir contribution.

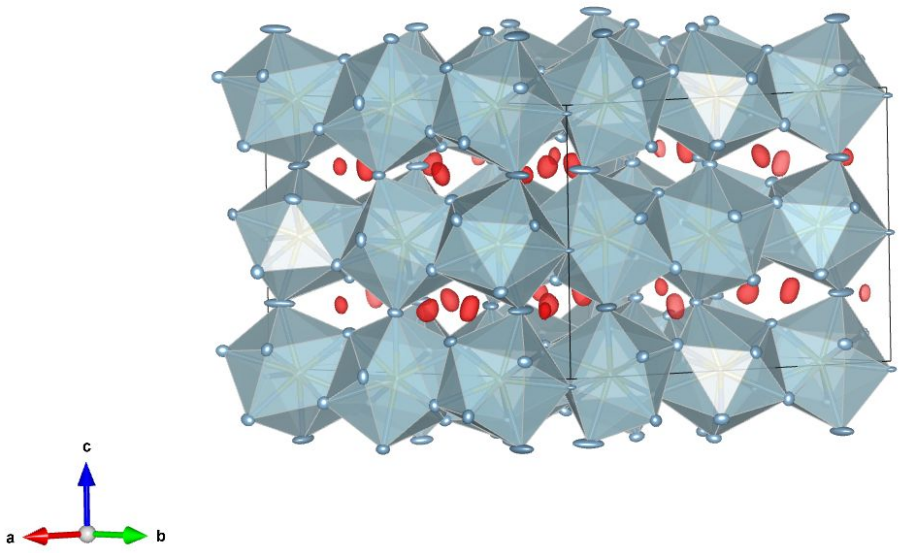

@ Figure 10: Electron Localization function, showing the isodensity larger than 0.7 (in red) between two aluminum atoms

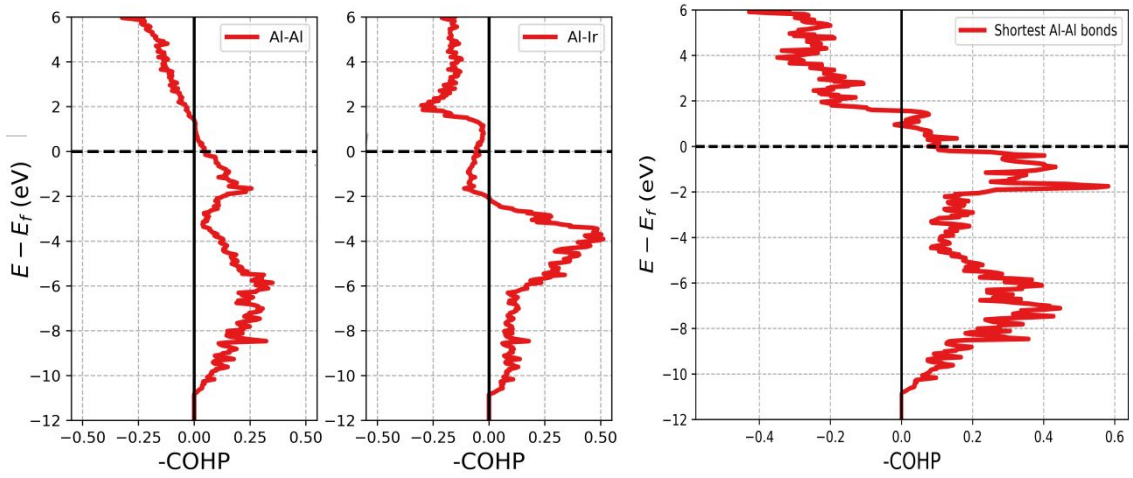

(a) (b)

@Fig. 11 : (a) COHPs for Al-Al and Al-Ir bonds averaged over all Al-Al and Al-Ir bonds shorter than 3A ; (b) COHPs for the shortest Al-Al bonds (2.640 Å)

Table

Table 1 : Crystallographic data for Al4Ir

Chemical formulae	$Al_{3.99}Ir$	
Formula weight (g/mol)	300.14	
Wavelength	0.71073 Å	
Crystal dimensions(mm)	0.01 x 0.012 x 0.023	
Space Group	*P3c1*(158)	
Unit cell dimensions (Å)	Experimental a=12.8802(2) Å c=9.8130(2) Å V = 1409.87(5)Å^3	VASP a=12.92 Å c=9.87 Å V = 1426.83Å^3
Z	18	
Calculated density	6.363g/cm^3	
Absorption Coefficient	43.429 mm^{-1}	
θ range for data collection(deg)	1.83 à 51.63°	
	-27<h<27, -27<k<28, -21<l<21	
Reflections observed/Independant/I>2σ	93424/10551/8180	
R_{int}	0.128	
Absorption correction	SADABSV2012/1 multiscan	
Resolution program	Direct method SHELXS-97(Sheldrick, 2008)	
Goodness of fit on F^2	1.026	
Number of variables	137	
R1/wR2(observed- I>2σ)	0.0444/0.0959	
R1/wR2(all)	0.067/0.1095	
$\Delta\rho_{max}$, $\Delta\rho_{min}$(eÅ^{-3})	7.238 , -4.164	

Table 2 Experimental Atomic coordinates and isotropic displacement parameters, the number in italic correspond to the atomic coordinate after relaxation.

Atom name	Wyckoff position	occupation	x/a	y/b	z/c	Ueq(Å^2)
Ir1	6d	1	0.79947(4) *0.80041*	0.55810(3) *0.55816*	0.98188(3) *0.98248*	0.00612(7)
Ir2	6d	1	0.77449(4) *0.77439*	0.89254(5) *0.89294*	0.99804(3) *0.99848*	0.00628(7)
Ir3	6d	1	0.43051(5) *0.42992*	0.89237(4) *0.8924*	0.98919(7) *0.9898*	0.00598(5)
Al1	6d	1	0.9475(3) *0.9483*	0.5280(3) *0.5276*	0.8300(4) *0.8285*	0.0104(5)
Al2	6d	1	0.9434(3) *0.9444*	0.7337(3) *0.7328*	0.8390(4) *0.8372*	0.0095(5)
Al3	6d	1	0.9038(3) *0.9029*	0.7672(2) *0.7671*	0.5827(4) *0.5813*	0.0088(5)
Al4	6d	1	0.8875(3) *0.8867*	0.4731(3) *0.4734*	0.5735(4) *0.5722*	0.0088(5)
Al5	6d	0.97(2)	0.8327(5) *0.8414*	0.8805(4) *0.8873*	0.7498(4) *0.7501*	0.0178(8)
Al6	6d	1	0.7271(4) *0.7250*	0.5131(4) 0.5101	0.7337(4) 0.7345	0.0155(7)
Al7	6d	1	0.6779(3) *0.6798*	0.6668(3) *0.6680*	0.8874(4) *0.8855*	0.0101(6)
Al8	6d	1	0.3327(3) *0.33313*	0.9843(3) *0.98442*	0.5996(4) *0.60262*	0.0088(5)
Al9	6d	1	0.6200(3) *0.6206*	0.8947(4) *0.8952*	0.6480(4) *0.6499*	0.0101(5)
Al10	6d	1	0.5606(3) *0.5606*	0.8049(3) *0.8046*	0.9062(4) *0.9063*	0.0088(5)
Al11	6d	1	0.3872(3) *0.3853*	0.8202(3) *0.8188*	0.7377(4) *0.7383*	0.0102(5)
Al12	2c	1	1/3	2/3	0.0163(6) *0.0167*	0.0089(8)
Al13	2b	1	2/3	1/3	0.9424(7) *0.9396*	0.0093(9)
Al14	2a	1	0.0	0.0	0.9715(7) *0.9705*	0.0105(9)

Table 3 : Anisotropic atomic displacement parameters (Å^2) for Al_4Ir

Atoms	U(1,1)	U(2,2)	U(3,3)	U(2,3)	U(1,3)	U(1,2)
Ir1	0.00630(12)	0.00620(13)	0.00546(13)	0.00000(8)	0.00019(10)	0.00285(9)
Ir2	0.00635(12)	0.00726(13)	0.00550(12)	0.00047(10)	0.00022(8)	0.00364(10)
Ir3	0.00648(11)	0.00607(10)	0.00547(9)	0.00020(8)	0.00031(9)	0.00324(9)

Al1	0.0105(13)	0.0138(13)	0.0082(12)	-0.0006(10)	-0.0016(10)	0.0072(11)
Al2	0.0103(13)	0.0079(11)	0.0085(13)	0.0003(9)	-0.0008(9)	0.0031(10)
Al3	0.0063(11)	0.0097(12)	0.0080(12)	-0.0012(10)	-0.0007(9)	0.0022(10)
Al4	0.0084(12)	0.0107(13)	0.0089(13)	0.0011(10)	0.0017(9)	0.0058(10)
Al5	0.033(3)	0.024(2)	0.0051(14)	-0.0021(12)	-0.0002(14)	0.024(2)
Al6	0.0145(15)	0.028(2)	0.0049(13)	-0.0013(12)	-0.0004(10)	0.0111(15)
Al7	0.0080(12)	0.0103(14)	0.0112(16)	0.0005(10)	0.0006(10)	0.0040(11)
Al8	0.0086(12)	0.0079(12)	0.0096(14)	-0.0011(9)	0.0001(9)	0.0041(10)
Al9	0.0100(12)	0.0156(14)	0.0067(12)	0.0016(10)	0.0013(9)	0.0079(11)
Al10	0.0076(11)	0.0091(12)	0.0095(13)	-0.0003(9)	-0.0007(9)	0.0042(10)
Al11	0.0104(12)	0.0127(13)	0.0065(11)	-0.0011(10)	0.0000(10)	0.0050(10)
Al12	0.0068(11)	0.0068(11)	0.013(2)	0.000	0.000	0.0034(6)
Al13	0.0067(12)	0.0067(12)	0.015(2)	0.000	0.000	0.0034(6)
Al14	0.0073(12)	0.0073(12)	0.017(3)	0.000	0.000	0.0037(6)

The anisotropic atomic displacement factor exponent takes the form: $-2\pi^2[h^2 a^{*2} U_{11} + ... + 2 h k a^* b^* U_{12}]$

Table 4 : Bärnighausen diagram showing the relationship between $AuIrAl_3$ (*P-3m1*) and Al_4Ir (*P3c1*) throught (*P-3c1*)

$AuIrAl_3$ *P-3m1* (164)			*P-3c1* (165)			Al_4Ir *P3c1* (158)		
Al	1a	0 0 0	Al	2b	0 0 0	Al	6d	X1,Y1,Z1
					0 0 1/2		6d	X2,Y2,Z2
							6d	X3,Y3,Z3
Al	2d	1/3 2/3 0.64	Al	4d	1/3 2/3 z1	Al	6d	X4,Y4,Z4
					2/3 1/3,1/2-z1		2c	2/3,1/3,Z5
					2/3 1/3 –z1		6d	X6,Y6,Z6
					1/3 2/3 ½+z1		2a	0,0,Z7
							2b	1/3,2/3,Z8
							6d	X9,Y9,Z9
							6d	X10,Y10,Z10
							6d	X11,Y11,Z11
Au,Ir	2d	1/3 2/3 0.16	Al	4d	1/3 2/3 z2	Au,Ir	6d	X12,Y12,Z12
					2/3 1/3 ½-z2		2c	2/3,1/3,Z13

					2/3 1/3 –z2		6d	X14,Y14,Z14
					1/3 2/3 ½+z2		2a	0,0,Z15
							2b	1/3,2/3,Z16
							6d	X17,Y17,Z17
							6d	X18,Y18,Z18
							6d	X19,Y19,Z19